

# Extinction Profiles Fusion for Hyperspectral Images Classification

Leyuan Fang, *Senior Member, IEEE*, Nanjun He, *Student Member, IEEE*, Shutao Li<sup>id</sup>, *Senior Member, IEEE*, Pedram Ghamisi<sup>id</sup>, *Member, IEEE*, and Jón Atli Benediktsson<sup>id</sup>, *Fellow, IEEE*

**Abstract**—An extinction profile (EP) is an effective spatial–spectral feature extraction method for hyperspectral images (HSIs), which has recently drawn much attention. However, the existing methods utilize the EPs in a stacking way, which is hard to fully explore the information in EPs for HSI classification. In this paper, a novel fusion framework termed EPs-fusion (EPs-F) is proposed to exploit the information within and among EPs for HSI classification. In general, EPs-F includes the following two stages. In the first stage, by extracting the EPs from three independent components of an HSI, three complementary groups of EPs can be constructed. For each EP, an adaptive superpixel-based composite kernel strategy is proposed to explore the spatial information within an EP. The weights to create the composite kernel and the number of superpixels are automatically determined based on the spatial information of each EP. In the second stage, since the different EPs contain highly complementary information, a simple yet effective decision fusion method is further applied to obtain the final classification result. Experiments on three real HSI data sets verify the qualitative and quantitative superiority of the proposed EPs-F method over several state-of-the-art HSI classifiers.

**Index Terms**—Classification, composite kernel, decision fusion, extinction profile (EP), hyperspectral image (HSI).

## I. INTRODUCTION

CLASSIFICATION of hyperspectral images (HSIs) has many applications, including the precision agriculture [1], urban mapping [2], and national defense [3]. In HSIs, each pixel is a high-dimensional vector, and its entries represent the spectral responses of different spectral bands, which incorporate abundant spectral information to achieve high classification accuracy.

Manuscript received March 19, 2017; revised May 31, 2017, August 20, 2017, and October 2, 2017; accepted October 24, 2017. Date of publication November 22, 2017; date of current version February 27, 2018. This work was supported in part by the National Natural Science Fund of China for Distinguished Young Scholars under Grant 61325007, in part by the National Natural Science Fund of China for International Cooperation and Exchanges under Grant 61520106001, in part by the National Natural Science Foundation under Grant 61771192, and in part by the Fund of Hunan Province for Science and Technology Plan Project under Grant 2017RS3024. (*Corresponding author: Shutao Li.*)

L. Fang, N. He, and S. Li are with the College of Electrical and Information Engineering, Hunan University, Changsha 410082, China (e-mail: fangleyuan@gmail.com; henanjun@hnu.edu.cn; shutao\_li@hnu.edu.cn).

P. Ghamisi is with the German Aerospace Center, Remote Sensing Technology Institute, 82234 Wessling, Germany, and also with the Technische Universität München, Signal Processing in Earth Observation, 80333 München, Germany (e-mail: pedram.ghamisi@dlr.de).

J. A. Benediktsson is with the Faculty of Electrical and Computer Engineering, University of Iceland, 101 Reykjavik, Iceland (e-mail: benedikt@hi.is).

Color versions of one or more of the figures in this paper are available online at <http://ieeexplore.ieee.org>.

Digital Object Identifier 10.1109/TGRS.2017.2768479

In recent years, a number of classifiers have been introduced for HSI classification, including the neural networks [4], multiple kernel methods [5]–[7], collaborate representation [8], [9], and sparse representation [10]–[13], since they are widely used in many applications [14], [15]. Among these methods, support vector machines (SVMs) [16], [17] have shown good performance especially when a limited number of training samples are available [18]. In general, the traditional SVM method classifies the image without considering the contextual information, i.e., interpixel dependence. Therefore, the classification map obtained by the SVM method may contain much salt and pepper noise. To enhance the classification performance, the composite kernel-based SVMs were utilized to combine both the spectral and spatial information [19]–[21]. Camps-Valls *et al.* [19] constructed a family of composite kernels by utilizing Mercer’s kernels, which can explore the spatial information in an efficient way. Moreover, in [20], a generalized composite kernel framework was proposed to combine the spectral and spatial information by a kernel stacking manner.

On the other hand, various feature extraction-based classification methods have been proposed [22]–[25]. In [23], principal component analysis (PCA) was utilized for feature extraction. In [24] and [25], independent component analysis (ICA) and linear discriminative analysis have been investigated for discriminative feature extraction. In general, these methods are designed only for spectral feature extraction, without considering the spatial dependences of adjacent pixels. To enhance the classification performance, spatial information should also be considered. A considerable number of spatial–spectral feature extraction-based classification methods have been developed in the literatures, including the classical Markov random field modeling-based methods [26], [27], morphological profile-based methods [28], its extended versions [29], [30], morphological attribute profile (AP) [31], and extinction profile (EP) [32], [33].

Among these feature extraction methods, the EP has recently drawn much attention, since it has the following advantages. First, it can simultaneously preserve the geometrical characteristics of the input image, while removing unimportant details. Second, it can deliver a better recognition performance than the traditional spatial–spectral AP [32] feature extraction method. To apply the EP method to the HSI, the ICA is used to extract a few informative features from the HSI and the three main independent components (ICs) of the HSI are preserved as the base images to produce EPs.

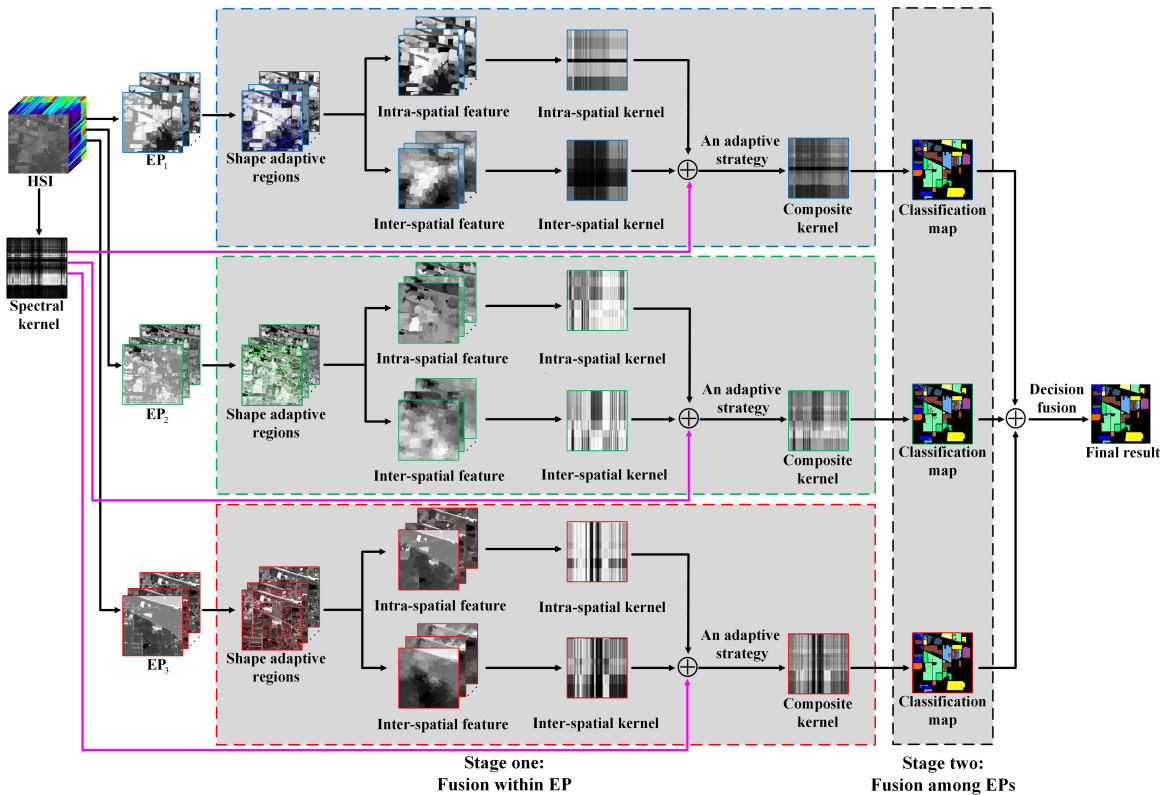


Fig. 1. Flowchart of the proposed EPs-F algorithm.

Since the ICA method aims at minimizing the dependence between its components [34], the obtained three EPs (denoted by  $EP_1$ ,  $EP_2$ , and  $EP_3$ ) are relatively independent of each other, which can reflect the characteristics of the HSI from different aspects and offer highly complementary information among them. The procedure for the construction of three complementary EPs is illustrated in the second line of Fig. 1. As can be observed, since the important geometrical characteristics of ICs from HSIs are well preserved, there exists abundant spatial information within each EP. In addition, as the EPs are produced from relatively independent ICs, respectively, each EP has its own distinctive characteristics that can offer complementary information among EPs. Both the spatial-spectral information within and among EPs can be utilized to enhance the classification performance. However, the existing method simply stacks all EPs together [33], which cannot fully exploit these information in EPs for HSI classification.

In this paper, we propose a fusion framework termed EPs-F to exploit the information within and among the EPs for HSI classification. Generally, the proposed EPs-F method has two stages. In the first stage, to utilize the abundant spatial information within an EP, an adaptive superpixel-based composite kernel strategy is proposed to fuse two types of shape-adaptive spatial features of the EP and the spectral feature of the original HSI. Compared with other similar methods that need to set weights for different kernels manually, an adaptive strategy is proposed to produce the composite kernel based on the spatial information. Moreover, an automatic approach is proposed to determine the number of superpixels based on

the contextual information of the EP. In the second stage, since different EPs reflect the HSI in different aspects that can provide complementary information in the corresponding classification maps, a simple yet effective decision fusion method is considered to fuse the classification maps to get the final classification result.

The main contributions of this paper are listed as follows.

- 1) Different from the previous stacking strategy in [33], we propose an effective fusion framework to exploit the rich spatial information within an EP and highly complementary information among EPs for HSI classification.
- 2) To explore the spatial information within an EP, an adaptive superpixel-based composite kernel method is proposed, which can not only adaptively fuse the kernels of different features but also automatically select the number of superpixels.

The rest of this paper is organized as follows. In Section II, we briefly review the SVM method with a composite kernel for HSI classification, extinction filters, and the EP-based feature extraction method. The proposed EPs-F method is detailed in Section III. In Section IV, the experimental results compared with several state-of-the-art classification methods are given. Finally, in Section V, this paper is summarized and the future works are suggested.

## II. REVIEWS OF RELATED METHODS

In this section, we briefly review the SVM method with a composite kernel for HSI classification, the extinction filters (EFs), and the EP feature extraction method.

### A. SVM Method With Composite Kernel

Given a labeled training data set  $\{(x_1, y_1) \dots (x_n, y_n)\}$ , where  $x_i \in \mathbb{R}^N$  and  $y_i \in \{-1, +1\}$ , and a nonlinear mapping  $\phi(\cdot)$ , the SVM aims to solve the following classification problem:

$$\begin{aligned} \min_{w, \xi, b} & \left\{ \frac{1}{2} \|w\|_2 + C \sum_i \xi_i \right\} \\ \text{s.t. } & y_i (\langle \phi(x_i), w \rangle + b) \geq 1 - \xi_i, \quad \forall i = 1, \dots, n \\ & \xi_i > 0, \quad \forall i = 1, \dots, n \end{aligned} \quad (1)$$

where  $w$  and  $b$  define a linear classifier in the feature space.  $C$  is the regularization parameter to control the generalization capabilities of the classifier, and  $\xi_i$  are positive slack variables to cope with the outliers in training samples. The kernel trick is often adopted in the SVM with the kernel function defined as follows:

$$K(x_i, x_j) = \langle \phi(x_i), \phi(x_j) \rangle. \quad (2)$$

By incorporating (2) into (1), the final decision function for the test  $x$  can be obtained by solving its dual Lagrangian problem, which is shown as follows:

$$f(x) = \text{sgn} \left( \sum_{i=1}^n y_i \alpha_i K(x_i, x) + b \right) \quad (3)$$

where  $\alpha_i$  are the Lagrange multipliers. For HSI classification, the *one-against-one* multiclassification scheme is adopted in the SVM method [19]. To further exploit the spatial information in an HSI, the composite kernel strategy is adopted. Assume that the original training spectral pixels and spatial features are  $(x_1^{\text{spe}}, \dots, x_n^{\text{spe}})$  and  $(x_1^{\text{spa}}, \dots, x_n^{\text{spa}})$ , respectively, then two types of kernels can be constructed (i.e., spectral kernel and spatial kernel denoted by  $K_{\text{spe}}(x_i^{\text{spe}}, x_j^{\text{spe}})$  and  $K_{\text{spa}}(x_i^{\text{spa}}, x_j^{\text{spa}})$  [19], respectively). The composite kernel is computed by a weighted average operation

$$K_{\text{CW}}(x_i, x_j) = \mu_{\text{spe}} K_{\text{spe}}(x_i^{\text{spe}}, x_j^{\text{spe}}) + \mu_{\text{spa}} K_{\text{spa}}(x_i^{\text{spa}}, x_j^{\text{spa}}) \quad (4)$$

where  $\mu_{\text{spe}}$  and  $\mu_{\text{spa}}$  are the weights for the spectral kernel  $K_{\text{spe}}(x_i^{\text{spe}}, x_j^{\text{spe}})$  and the spatial kernel  $K_{\text{spa}}(x_i^{\text{spa}}, x_j^{\text{spa}})$ , respectively, and  $\mu_{\text{spe}} + \mu_{\text{spa}} = 1$ . The composite kernel is introduced into (3) to create a new decision rule for classification. Compared with a single kernel, since the spatial information and spectral information of the HSI are jointly considered, the composite kernel can provide a better classification performance. Among various kernel functions, the radial basis function (RBF) kernel is widely used, which is computed as

$$K(x_i, x_j) = \exp(-\|x_i - x_j\|^2 / 2\sigma^2). \quad (5)$$

### B. Extinction Filters

The EFs are connected filters, which preserve the relevant image extrema. Relevance is measured by the concept of extinction values defined in [36]. The EFs are defined as follows: let  $\max(\mathbf{F}) = \{M_1, M_2, \dots, M_N\}$  denote the regional maxima of image  $\mathbf{F}$ . Each regional maxima  $M_i$  has an extinction value  $\varepsilon_i$  corresponding to the increasing attribute being

analyzed. The EF of  $\mathbf{F}$  preserves the  $n$  maxima with the highest extinction values, i.e.,  $\text{EF}^n(\mathbf{F})$ , which is given as follows:

$$\text{EF}^n(\mathbf{F}) = R_{\mathbf{F}}^\delta(\mathbf{G}) \quad (6)$$

where  $R_{\mathbf{F}}^\delta(\mathbf{G})$  is the reconstruction by dilation [37] of the mask image  $\mathbf{G}$ , which is given by  $\mathbf{G} = \max_{i=1}^n (M_i')$ . The  $\max$  is the pixelwise maximum operation.  $M_1'$  is the maximum with the highest extinction value, and  $M_2'$  has the second highest extinction value.

### C. Extinction Profile

The EP is composed of a sequence of thinning and thickening transformations obtained by a set of EFs with a sequence of progressively stricter criteria. For instance, an EP for the input grayscale image  $\mathbf{F}$  can be defined as follows:

$$\text{EP}(\mathbf{F}) = \left\{ \underbrace{\phi^{P_{\lambda,L}}(\mathbf{F}), \phi^{P_{\lambda,L-1}}(\mathbf{F}), \dots, \phi^{P_{\lambda,1}}(\mathbf{F}), \mathbf{F}}_{\text{thickening profile}}, \underbrace{\gamma^{P_{\lambda,L}}(\mathbf{F}), \gamma^{P_{\lambda,L-1}}(\mathbf{F}), \dots, \gamma^{P_{\lambda,1}}(\mathbf{F})}_{\text{thinning profile}} \right\} \quad (7)$$

with  $P_{\lambda,L} : \{P_{\lambda,i}\} (i = 1, \dots, L)$ , a set of  $L$  ordered predicates (i.e.,  $P_{\lambda,i} \subseteq P_{\lambda,k}, i \leq k$ ) [32].

In order to extract the EP from an HSI, the ICA, as mentioned above, is first utilized to obtain the most informative components and the three ICs are used as base images to produce EPs. Then, the EP method is applied on each IC as follows:  $\mathbf{EP}_1 = \text{EP}(\mathbf{IC}_1)$ ,  $\mathbf{EP}_2 = \text{EP}(\mathbf{IC}_2)$ , and  $\mathbf{EP}_3 = \text{EP}(\mathbf{IC}_3)$ . Since the ICs are relatively independent of each other [34], the obtained ICs can characterize the original HSI in different aspects that can offer distinctive and complementary information in the corresponding EP. The whole procedure of EPs extraction from ICs is shown in the first two lines of Fig. 1. In this way, three complementary EPs can be constructed.

## III. PROPOSED EPS-F METHOD

The framework of the proposed EPS-F method is summarized in the flowchart in Fig. 1, which includes the following two stages.

- 1) Within EP, an adaptive composite kernel strategy is proposed to fuse the spatial information of the EP and the spectral information of the HSI, and then the composite kernel is fed into an SVM to obtain the first stage classification maps.
- 2) Among EPs, since the classification maps from different EPs contain complementary information, the decision fusion is further adopted to fuse the classification maps for obtaining the final classification result.

### A. Stage I: Fusion Within EP

Stage I consists of the following steps: 1) the construction of shape-adaptive regions; 2) intra and intershape-adaptive spatial features extraction; and 3) an adaptive strategy for composite

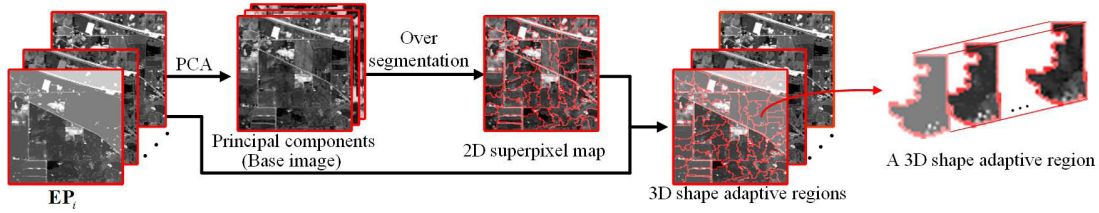


Fig. 2. Procedure for creating shape-adaptive regions  $i = 1, 2, 3$ .

kernel computation. Note that, to explore the abundant spatial information within each EP, one possible way is to use the fixed window based manner. However, there are some demerits associated with the fixed window. For example, on the edge structural area, the fixed size window might include the pixels from different classes, and thus, the spatial information of the EP cannot be sufficiently utilized. Recent work [35] has demonstrated that the superpixel can adjust the shape of the window based on the contextual information, which can more effectively explore the spatial information. Moreover, since the HSIs have more than 100 spectral bands and some bands may have heavy noise or artifacts, directly segmenting the whole HSIs with the superpixel method [38]–[40] will create very high computational cost and also be interfered by the noise existed in the spectral bands. To address this issue, our method applies the PCA [44] on the HSI, and extract the first three PCs as the based images for superpixel segmentation, which can greatly reduce the computational cost and is robust to noise. According to the aforementioned analysis, for each EP, an oversegmentation-based superpixel method [35] is applied on the first three PCs to create shape-adaptive regions for spatial information extraction.

1) *Construction of Shape-Adaptive Regions*: The PCA [44] is first used to reduce the feature bands of the EP and the first three principal components are used as the base images (i.e.,  $\mathbf{I}^{\text{base}}$ ), since they contain the most important information of the EP. Then an oversegmentation method [35] is utilized to construct a 2-D superpixel map on the base image. Subsequently, the 2-D superpixel map that contains the position indexes of pixels within each superpixel is applied on the corresponding EP to extract the nonoverlapping 3-D shape-adaptive regions (denoted by  $\mathbf{Y}_t^{\text{shape}}$ ,  $t = 1, \dots, S^{\text{num}}$ , where  $S^{\text{num}}$  is the number of superpixels). The procedure for creating of shape-adaptive regions is illustrated in Fig. 2. As a result, we can construct many 3-D shape-adaptive regions for spatial feature extraction. More details about the oversegmentation algorithm can be found in [35].

Note that, in the superpixel segmentation part, the method to choose the number of superpixels is a key problem. Most of the existing methods [41]–[43] use a manual way to determine the number of superpixels for different images that are very time-consuming and are hard to be adaptable to other complex scenarios. To address this problem, we propose an adaptive strategy to determine this parameter by utilizing the contextual information. Specifically, the Canny filter [45] is utilized to detect the structural texture of the base image  $\mathbf{I}^{\text{base}}$  and the number of nonzero elements  $N^f$  in filtered images

(denoted by  $\mathbf{I}^{\text{filter}}$ ) is compared with the total number of pixels  $N^b$  in  $\mathbf{I}^{\text{base}}$  to create the texture ratio  $R$  by

$$R = \frac{N^f}{N^b}. \quad (8)$$

The number of superpixels  $S^{\text{num}}$  is computed by the predefined number of base superpixel  $S^{\text{base}}$  and the texture ratio  $R$  as follows:

$$S^{\text{num}} = S^{\text{base}} \times R. \quad (9)$$

For different EPs, the number of base superpixels is set to be fixed, while the texture ratio is automatically calculated based on the textural structures of the EPs by (8). Therefore, the superpixel number  $S^{\text{num}}$  can also be adaptively adjusted with the texture ratio  $R$ . In this way, not only the number of parameters is reduced but also the spatial characteristics of different features are considered.

2) *Intra and Intershape-Adaptive Spatial Features Extraction*: As can be seen in Fig. 2, each shape-adaptive region includes a group of neighbor pixels that are represented by  $y_t^k$ ,  $k = 1, \dots, K$ .  $K$  is the number of EP pixels within one shape-adaptive region. For each shape-adaptive region, we can extract two types of spatial features in the following two ways.

- 1) *Intrashape-Adaptive Spatial Feature*: To explore the spatial feature within a shape-adaptive region, we first compute the average of EP pixels ( $y_t^k$ ,  $k = 1, \dots, K$ ), which is denoted by  $\bar{y}_t$ . The average pixel  $\bar{y}_t$  is assigned to each EP pixel in  $\mathbf{Y}_t^{\text{shape}}$ . We perform the same operation for all the shape-adaptive regions. Therefore, a mean EP feature  $\mathbf{EP}^{\text{mean}}$  can be constructed by constituting all the filtered shape-adaptive regions.
- 2) *Intershape-Adaptive Spatial Feature*: By considering the neighboring shape-adaptive regions sharing the same spatial information, a weighted average strategy is applied on the neighboring shape-adaptive regions (i.e.,  $\mathbf{Y}_{t,v}^{\text{shape}}$ ,  $v = 1, \dots, J$ ) of the  $\mathbf{Y}_t^{\text{shape}}$ , where  $J$  is the number of its neighboring intershape-adaptive regions. The examples of shape-adaptive region  $\mathbf{Y}_t^{\text{shape}}$  and its neighboring shape-adaptive regions are represented in Fig. 3. The intershape-adaptive spatial feature is defined by (10). Specifically, the weighted average operation is applied on the average pixels  $\bar{y}_{t,v}$ ,  $v = 1, \dots, J$ , which are the average of  $\mathbf{Y}_{t,v}^{\text{shape}}$

$$y_t^{\text{weight}} = \sum_{v=1}^J w_{t,v} \times \bar{y}_{t,v} \quad (10)$$

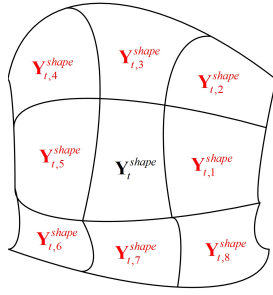


Fig. 3. Example of shape-adaptive region  $Y_t^{shape}$  and its neighbor shape-adaptive regions  $Y_{t,1}^{shape}, Y_{t,2}^{shape}, \dots, Y_{t,8}^{shape}$ .

where  $w_{t,v} = (\exp(-\|\bar{y}_t - \bar{y}_{t,v}\|_2^2/h)/\text{Sum})$ . Sum is defined as  $\sum_{v=1}^J \exp(-\|\bar{y}_t - \bar{y}_{t,v}\|_2^2/h)$ , and  $h$  is a predefined scalar. Moreover, the  $y_t^{weight}$  is assigned to all EP pixels in  $Y_t^{shape}$  and all shape-adaptive regions conducted the same operation. In this way, a weighted average EP feature  $EP^{weight}$  can be created.

3) *Adaptive Strategy for Composite Kernel Computation:* Assume that a set of spectral pixels (denoted by  $x_1^{spe}, \dots, x_N^{spe}$ , where  $N$  is the number of the training samples) are randomly (or manually) selected from the original HSI (denoted by  $X^{spe}$ ) as training samples. The position indexes of selected spectral pixels are then utilized to extract the corresponding spatial pixels from  $EP^{mean}$  (with mean EP pixels denoted by  $y_1^{mean}, \dots, y_N^{mean}$ ) and  $EP^{weight}$  (with weight average EP pixels denoted by  $y_1^{weight}, \dots, y_N^{weight}$ ), respectively. Thus, we can construct three types of feature training samples (denoted by  $x_1^{spec}, \dots, x_N^{spec}, y_1^{mean}, \dots, y_N^{mean}$ , and  $y_1^{weight}, \dots, y_N^{weight}$ , respectively). After that, the obtained three kinds of training samples are used to create three different kernels by the RBF kernel function in (5), that is

$$K_{spec}^{train}(x_i^{spe}, x_j^{spe}) = \exp(-\|x_i^{spe} - x_j^{spe}\|^2/2\sigma^2) \quad (11)$$

$$K_{intraEP}^{train}(y_i^{mean}, y_j^{mean}) = \exp(-\|y_i^{mean} - y_j^{mean}\|^2/2\sigma^2) \quad (12)$$

$$K_{interEP}^{train}(y_i^{weight}, y_j^{weight}) = \exp(-\|y_i^{weight} - y_j^{weight}\|^2/2\sigma^2). \quad (13)$$

Instead of manually selecting the weights of the above three kernels, an adaptive composite kernel strategy is proposed to adjust the weight automatically based on the contextual information of  $X^{spe}$ ,  $EP^{mean}$ , and  $EP^{weight}$ . Specifically, according to the complexness of the structural texture of  $I_s^{base}$ ,  $I_m^{base}$ , and  $I_w^{base}$  (i.e., the base image of  $X^{spe}$ ,  $EP^{mean}$ , and  $EP^{weight}$ , respectively), three texture ratios (i.e.,  $R_s$ ,  $R_m$ , and  $R_w$ ) can also be computed by (8). The filtered image is obtained by the Canny filter on the corresponding base image. Note that the base images are obtained by applying the PCA transform on the EP and only adopting the first three principal components. The obtained texture ratios are set as the weight of the

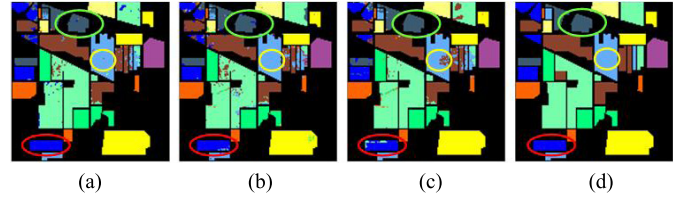


Fig. 4. Comparison between classification maps obtained from Fusion Stage I and the reference map. (a)–(c) Classification maps (i.e., map<sub>1</sub>, map<sub>2</sub>, and map<sub>3</sub>) obtained from EP<sub>1</sub>, EP<sub>2</sub>, and EP<sub>3</sub> in Fusion Stage I, respectively. (d) Reference map.

corresponding kernels, that is

$$K_{CW} = \frac{R_s}{\text{norm}} \times K_{spe}^{train}(x_i^{spe}, x_j^{spe}) + \frac{R_m}{\text{norm}} \times K_{intraEP}^{train}(y_i^{mean}, y_j^{mean}) + \frac{R_w}{\text{norm}} \times K_{interEP}^{train}(y_i^{weight}, y_j^{weight}) \quad (14)$$

where  $\text{norm} = R_s + R_m + R_w$ . In this way, the structural information of  $X^{spe}$ ,  $EP^{mean}$ , and  $EP^{weight}$  is well utilized in the composite kernel weights. Finally, the obtained composite kernel is incorporated into the SVM classifier to create the classification map of the test samples. The aforementioned operations are applied on each EP. Therefore, three complementary classification maps can be obtained, which are denoted by map<sub>1</sub>, map<sub>2</sub>, and map<sub>3</sub> (see the examples in Fig. 4).

### B. Stage II: Fusion Among EPs

Since each EP has its own distinctive characteristics that can reflect the original HSI in different aspects, the classification maps (i.e., map<sub>1</sub>, map<sub>2</sub>, and map<sub>3</sub>) obtained from different EPs have complementary information. For example, from Fig. 4, we can observe that the classification map<sub>1</sub> delivers the best classification performance in the red-circled area, whereas map<sub>2</sub> and map<sub>3</sub> show some wrong classifications in different parts of the red-circled area. The same situation can also be observed at other regions (e.g., the green-circled and the yellow-circled area). Thus, in this stage, the decision fusion is further utilized to fuse the three obtained classification maps for creating the final classification result. Specifically, majority voting (MV) is adopted in the three obtained classification maps (map<sub>1</sub>, map<sub>2</sub>, and map<sub>3</sub>) pixel by pixel. We count the number of each class occurrence and denote them as Count<sub>1</sub>, Count<sub>2</sub>, ..., Count<sub>M</sub>, where  $M$  is the class number. The class label of the test pixel can be obtained by

$$L = \max_m(\text{Count}_1, \text{Count}_2, \dots, \text{Count}_M). \quad (15)$$

In a very small number of cases, i.e., for a few test samples, the three classification maps' labels are different, which is hard to choose the right map's label as the final result. To address this issue, we define a *confidence level* with the initiation value be zero for each map (i.e., map<sub>1</sub>, map<sub>2</sub>, and map<sub>3</sub>). When one makes "majority" vote (i.e., its vote belongs to the majority vote), the *confidence level* of the corresponding map will increase by one. We finally choose the labels of

TABLE I  
NUMBERS OF SAMPLES IN DIFFERENT CLASSES IN THE THREE TEST IMAGES

Indian Pines			University of Pavia			Houston University Image					
Class	Name	Number	Class	Name	Number	Class	Name	Number	Class	Name	Number
1	Corn-notill	1428	1	Asphalt	6631	1	Healthy grass	1073	12	Parking Lot1	1233
2	Corn-mintill	830	2	Meadows	18649	2	Stressed grass	810	13	Parking Lot2	449
3	Grass-pasture	483	3	Gravel	2099	3	Synthetic grass	697	14	Tennis court	428
4	Grass-trees	730	4	Trees	3064	4	Tress	1053	15	Running track	660
5	Hay-windrowed	478	5	Metal sheet	1345	5	Soil	1242		Total	11099
6	Sybean-notill	972	6	Bare Soil	5029	6	Water	325			
7	Sybean-mintill	2455	7	Bitumen	1330	7	Residential	978			
8	Sybean-clean	593	8	Bricks	3682	8	Commercial	624			
9	Woods	1265	9	Shadows	947	9	Road	1031			
10	Bldg-grass-trees	386		Total	42776	10	Highway	382			
	Total	9620				11	Railway	114			

classification map that has the highest *confidence level* as the labels for those undetermined test samples.

#### IV. EXPERIMENTAL RESULTS AND DISCUSSION

The proposed EPs-F method is tested on three HSI images, i.e., the Airborne Visible/Infrared Imaging Spectrometer (AVIRIS) Indian Pines image, the Reflective Optics System Imaging Spectrometer (ROSIS-03) University of Pavia image, and the Houston University image. In addition, the classification results of the EPs-F method on the three test images are visually and quantitatively compared with several well-known HSI classification methods (i.e., the SVM [16], extended morphological profiles (EMP) [29], edge-preserving filter (EPF) [46], SVM-composite kernel (SVM-CK) [19], generalized composite kernel-based multivariate logistic regression (GCK-MLR) [20], superpixel-based classification via multiple kernels (SC-MK) [21], multiple nonlinear feature learning with multivariate logistic regression (MNFL) [47], and EPs with a stacking manner (EPs-stacking) [33]). The SVM is a pixelwise classification method, which does not consider spatial information. For the EMP and EPF methods, the spatial context of the HSI was exploited by the morphological method and edge-filtering, respectively. In the SVM-CK method, the mean of the neighborhood pixels in a fixed window was utilized to extract the spatial features, and then the spatial features were combined with spectral features using a weighted composite kernel. The weights in the SVM-CK were manually selected. The SC-MK method adopted a superpixel method to extract both the spatial and spectral information. In the GCK-MLR method, a generalized composite kernel that fused the spectral-spatial information was constructed for HSI classification. For the MNFL method, various features extracted from HSI were combined together for classification. For the EPs-stacking method, the different EPs are used in a stacking way that is hard to fully explore the information in EPs. To objectively evaluate the classification results, three metrics of overall accuracy (OA), average accuracy (AA), and Kappa coefficient ( $K$ ) are adopted. Besides, the average and standard deviation of the classification accuracies over ten runs are reported. The code of the proposed EPs-F method will be released on the Website.<sup>1</sup>

<sup>1</sup><https://sites.google.com/site/leyuanfang/home>

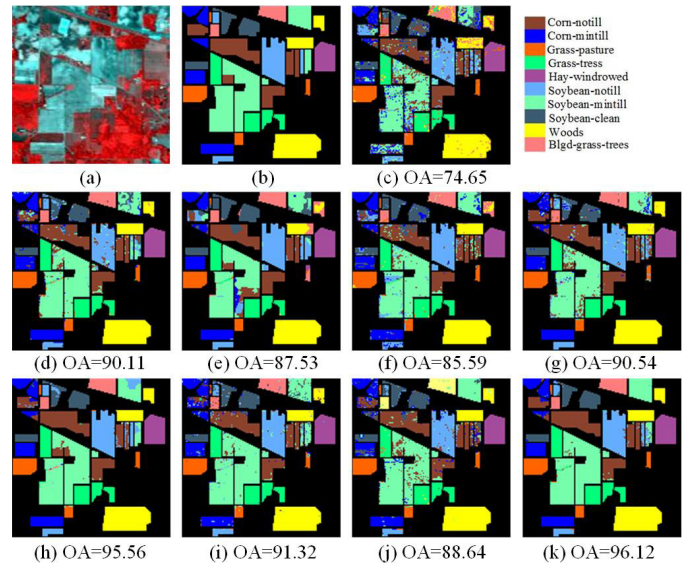


Fig. 5. Reference map and classification results (%) for the Indian Pines image. (a) False-color composite images. (b) Reference. (c) SVM [16]. (d) EMP [29]. (e) SVM-CK [19]. (f) EPF [46]. (g) GCK-MLR [20]. (h) SC-MK [21]. (i) MNFL [47]. (j) EPs-stacking [33]. (k) Proposed EPs-F.

#### A. Experimental Data Sets

1) *AVIRIS Indian Pines*: The Indian Pines image was acquired by the AVIRIS sensor over the agricultural Indian Pines site in northwestern Indiana. The size of this image is  $145 \times 145 \times 220$ , where 20 water absorption bands are removed. The spatial resolution of the image is 20 m/pixel and the spectral coverage ranges from 200 to 240 nm. The reference map of this image contains 16 classes, most of which are different kinds of crops. In our experiment, the major ten classes are used and the reference classes are reported in Table I. Fig. 5(a) and (b) demonstrates the false-color composite of the Indian Pines image and the corresponding reference data.

2) *University of Pavia*: The University of Pavia image was captured by the ROSIS-03 sensor over an urban area surrounding the University of Pavia, Italy. The ROSIS-03 sensor generated an image with a geometric resolution of 1.3 m/pixel with the spectral coverage ranging from 430 to 860 nm. This image is of size  $610 \times 340 \times 103$ , where 12 spectral bands

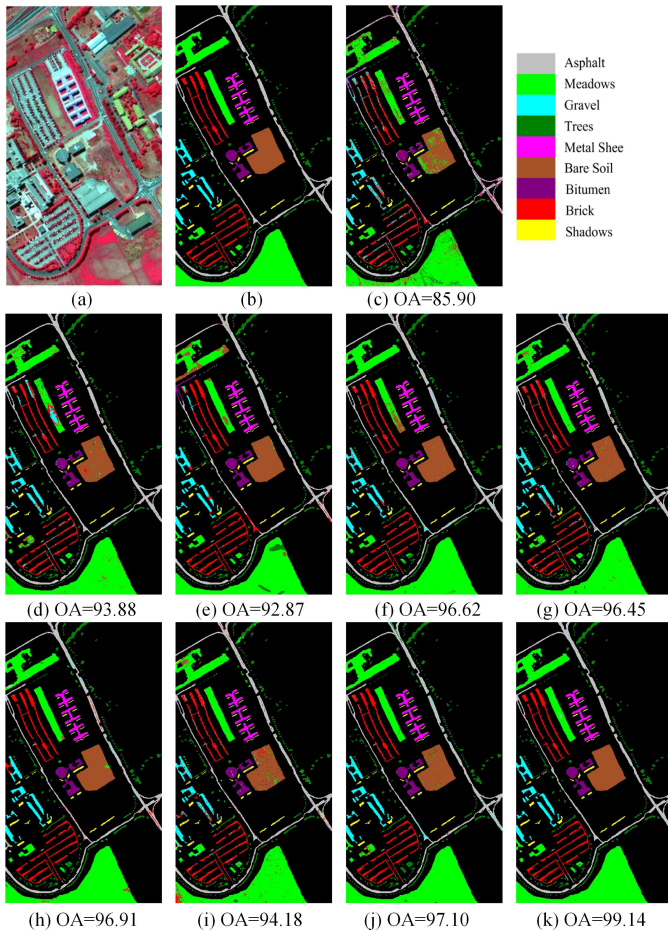


Fig. 6. Reference map and classification results (%) for the University of Pavia image. (a) False-color composite images. (b) Reference. (c) SVM [16]. (d) EMP [29]. (e) SVM-CK [19]. (f) EPF [46]. (g) GCK-MLR [20]. (h) SC-MK [21]. (i) MNFL [47]. (j) EPs-stacking [33]. (k) Proposed EPs-F.

are removed due to the existence of high noise. The reference of this image contains nine ground-truth classes and reference classes are represented in Table I. Fig. 6(a) and (b) shows the false-color composite of the University of Pavia image and the corresponding reference data.

3) *Houston University*: The Houston University image was acquired over the Houston University campus and its neighboring area, which was used in the 2013 GRSS Data Fusion Contest. The hyperspectral data contain 144 spectral bands in the 380–1050-nm region, and  $349 \times 1905$  pixels with a spatial resolution of 2.5 m. This image is an urban data sets whose most of the land covers are man-made objects that contain 15 classes. The reference classes are also shown in Table I. Fig. 7(a) and (b) shows the false-color composite of the Houston University image and the corresponding reference data.

### B. Parameter Setting

For the tested Indian Pines, University of Pavia, and Houston University images, the number of base superpixels is set to 1750, 5000, and 45 000, respectively. The parameter  $h$  in (10) is set to 500. The effects of the number of base

superpixels and  $h$  are discussed in Section IV-C. The  $\sigma$  in (11)–(13) is set to 1 and the parameters of the SVM classifier in our method are selected by a fivefold cross-validation technique. The parameters of the other test methods are set as follows.

- 1) The parameters of the SVM method are determined by the fivefold cross-validation technique.
- 2) For the SVM-CK method, the summation composite kernel is used to make a decision rule, in which the weights of the spectral content and textural content are set as the optimal value in [21]. The parameters of the SVM classifier used in the SVM-CK method are also selected by the fivefold cross-validation technique.
- 3) The parameters of the EMP, EPF, GCK-MLR, MNFL, EPs-stacking, and SC-MK are set as the defaulted values reported in [29], [46], [19], [47], [33], and [21], respectively.

### C. Results Comparison

Fig. 5 shows different classification maps obtained by different investigated methods on the Indian Pines image with 50 training samples randomly selected for each class ( $Tr = 50$ ). As can be observed, by only considering the spectral information, the SVM method shows a very noisy estimation in its classification map. By incorporating the local spatial context of the HSI, the EMP, SVM-CK, EPF, and GCK-MLR deliver a smoother visual result. However, those approaches still fail to identify the pixels in the detailed and edge regions (e.g., the seventh class, Soybeans-mintill). In addition, by combining various spatial features (e.g., non-linear and linear features of the HSI) or extracting the spatial information of the HSI with a more sophisticated strategy, the MNFL and SC-MK methods have better visual performance, but still existing some wrong classification labels (e.g., the fourth class, area of grass tree). Since the rich spatial information in EPs cannot be fully explored by a simple stacking manner, the EPs-stacking method also fails to classify the pixels in some area (e.g., the seventh class, Sybean-mintill). By contrast, the proposed EPs-F method has the best visual classification performance, which not only reduces the noise greatly but also preserves the meaningful structural information. The corresponding classification accuracies are reported in Table II with the best results in bold. As can be seen, the proposed method achieves the highest classification accuracy in terms of OA, AA, and K.

Fig. 6. illustrates different classification maps obtained by different test methods on the University of Pavia image with 50 training samples randomly selected per class ( $Tr = 50$ ). As can be observed from Fig. 6, the SVM classification map is still very noisy. The EMP, SVM-CK, and MNFL can deliver a comparatively smooth result, but still fail to detect some meaningful regions (e.g., the detailed or near-edge areas). Although, the EPF, GCK-MLR, and SC-MK algorithms show improvements on the detection of the details, there is still a noticeable salt and pepper noise in the large-scale green area (e.g., second class, meadows, at the bottom of the classification map). The same situation can also be observed on the area of

TABLE II  
AA (STANDARD DEVIATION) (%) OF TEN REPEATED EXPERIMENTS ON THE INDIAN PINES IMAGE OBTAINED BY DIFFERENT METHODS WITH 50 TRAINING SAMPLES PER CLASS

Class	SVM [16]	EMP [29]	EPF [46]	SVM-CK [19]	GCK-MLR [20]	SC-MK [21]	MNFL [47]	EPs-stacking [33]	EPs-F
1	63.87(3.69)	83.17(4.40)	84.47(6.02)	78.24(6.91)	78.70(3.97)	<b>93.80</b> (3.63)	91.13(2.80)	82.02(1.15)	90.71(3.29)
2	53.43(4.70)	84.47(5.48)	87.23(9.66)	84.15(3.58)	91.56(2.13)	95.41(1.83)	91.01(3.01)	83.85(7.07)	<b>95.45</b> (3.16)
3	83.46(3.76)	89.85(3.71)	97.09(2.04)	93.95(3.22)	92.21(2.04)	97.16(2.16)	92.20(1.98)	94.78(1.80)	<b>98.45</b> (0.76)
4	92.41(1.69)	97.18(0.86)	96.85(1.66)	98.47(1.80)	98.79(0.67)	99.85(0.01)	91.25(0.54)	98.06(0.94)	<b>99.96</b> (0.01)
5	96.78(1.71)	99.98(0.06)	98.70(1.84)	99.86(0.04)	99.98(0.06)	<b>100</b> (0)	92.81(0.25)	99.72(0.03)	<b>100</b> (0)
6	63.66(3.91)	84.03(5.08)	75.50(5.27)	77.53(2.36)	85.07(2.23)	94.99(3.74)	92.03(2.91)	85.03(3.44)	<b>96.17</b> (1.71)
7	81.36(2.41)	92.66(2.26)	<b>95.93</b> (2.86)	75.07(2.87)	85.38(2.10)	90.61(2.73)	93.49(1.71)	81.23(5.31)	93.67(3.78)
8	49.19(2.28)	73.51(1.94)	72.50(4.98)	79.89(2.79)	90.33(2.70)	96.28(1.75)	90.98(1.51)	83.61(6.03)	<b>96.94</b> (1.88)
9	95.53(0.91)	99.86(0.14)	99.43(0.38)	92.35(1.71)	98.35(0.95)	98.47(0.05)	91.74(1.60)	97.66(1.04)	<b>99.79</b> (0.01)
10	55.21(4.70)	95.32(2.15)	73.99(9.57)	94.40(3.10)	95.60(2.81)	98.42(0.60)	91.85(3.66)	97.62(1.97)	<b>99.70</b> (0.02)
OA	72.73(0.85)	89.43(1.67)	88.31(1.80)	83.68(2.35)	89.36(0.70)	95.06(0.67)	90.86(0.80)	87.66(1.93)	<b>95.80</b> (0.46)
AA	68.72(0.93)	87.76(1.90)	86.51(2.01)	87.39(1.81)	91.71(0.40)	96.50(0.40)	91.85(0.78)	90.43(1.47)	<b>97.09</b> (0.24)
K	73.52(0.61)	90.01(1.62)	88.22(1.53)	81.14(2.64)	87.73(0.82)	94.32(0.81)	89.44(0.91)	85.89(2.21)	<b>95.22</b> (0.52)

TABLE III  
AA (STANDARD DEVIATION) (%) OF TEN REPEATED EXPERIMENTS ON THE UNIVERSITY OF PAVIA IMAGE OBTAINED BY DIFFERENT METHODS WITH 50 TRAINING SAMPLES PER CLASS

Class	SVM [16]	EMP [29]	EPF [46]	SVM-CK [19]	GCK-MLR [20]	SC-MK [21]	MNFL [47]	EPs-stacking [33]	EPs-F
1	93.79(3.69)	<b>98.61</b> (0.96)	98.00(0.60)	88.23(3.32)	95.68(0.68)	95.37(1.50)	95.92(1.11)	94.48(1.53)	98.03(0.72)
2	94.44(4.70)	<b>98.62</b> (1.05)	98.43(1.03)	92.60(3.83)	97.38(1.56)	95.62(1.35)	95.90(1.53)	95.79(1.89)	98.27(1.10)
3	67.87(3.76)	73.73(0.83)	92.18(7.45)	85.75(2.76)	91.91(2.81)	97.76(1.61)	84.76(3.50)	97.40(0.78)	<b>99.39</b> (0.07)
4	81.98(1.69)	96.09(1.01)	91.87(8.31)	94.15(1.78)	95.09(1.11)	96.34(1.21)	95.32(1.49)	98.79(0.89)	<b>98.01</b> (0.83)
5	95.00(1.71)	98.89(0.18)	97.55(3.11)	99.52(0.09)	99.21(0.21)	<b>99.96</b> (0.06)	99.49(0.24)	99.52(0.19)	99.94(0.04)
6	62.89(3.91)	85.79(4.22)	80.13(8.67)	91.46(2.16)	97.03(0.89)	97.78(1.66)	96.41(0.84)	96.65(0.66)	<b>99.90</b> (0.07)
7	60.10(2.41)	94.62(0.62)	86.99(7.29)	92.47(2.80)	97.86(0.97)	99.95(0.02)	98.99(0.68)	97.62(0.75)	<b>99.96</b> (0.05)
8	81.20(5.98)	92.31(1.45)	91.47(7.86)	83.39(4.21)	93.14(2.95)	<b>94.84</b> (2.74)	87.57(3.01)	97.16(1.76)	<b>99.14</b> (0.36)
9	99.91(0.02)	99.79(0.03)	98.91(0.71)	99.96(0.01)	99.77(0.14)	<b>99.99</b> (0.01)	99.83(0.11)	98.13(1.11)	<b>99.99</b> (0.06)
OA	84.06(1.09)	94.57(0.77)	93.57(2.39)	91.14(1.06)	96.40(0.36)	96.28(1.48)	94.95(0.72)	96.76(0.59)	<b>98.67</b> (0.67)
AA	79.35(1.26)	92.85(1.01)	91.60(3.03)	91.95(0.61)	96.34(0.31)	97.51(0.70)	94.91(0.36)	97.53(0.28)	<b>99.18</b> (0.18)
K	82.02(0.91)	93.21(1.02)	92.82(2.55)	88.34(1.37)	95.24(0.51)	95.11(1.91)	93.43(0.91)	95.68(0.76)	<b>98.23</b> (0.93)

TABLE IV  
AA (STANDARD DEVIATION) (%) OF TEN REPEATED EXPERIMENTS ON THE HOUSTON UNIVERSITY IMAGE WITH VARIOUS TRAINING SAMPLES OBTAINED BY DIFFERENT METHODS

Method	$Tr=10$			$Tr=30$			$Tr=50$		
	OA	AA	K	OA	AA	K	OA	AA	K
SVM [16]	74.05(2.07)	71.97(2.20)	75.21(0.16)	86.35(1.14)	85.24(1.22)	86.23(1.01)	89.93(0.63)	89.10(0.68)	89.83(0.72)
EMP [29]	78.50(2.22)	76.79(2.38)	80.44(2.02)	88.03(0.58)	87.07(0.62)	88.62(0.73)	92.25(0.60)	91.62(0.65)	92.41(0.52)
EPF [46]	78.73(2.42)	77.02(2.59)	78.22(2.02)	91.35(0.97)	90.65(1.04)	91.02(1.31)	94.55(0.80)	94.10(0.86)	94.41(1.02)
SVM-CK [19]	77.04(2.03)	78.46(1.68)	75.19(2.17)	88.95(1.49)	89.62(1.56)	88.05(1.56)	92.27(0.42)	92.63(0.43)	91.04(0.46)
GCK-MLR [20]	80.45(1.54)	81.72(1.20)	78.91(1.71)	91.66(1.07)	91.90(0.89)	91.01(1.12)	94.41(0.49)	94.45(0.50)	94.01(0.53)
SC-MK [21]	74.84(3.19)	77.80(2.91)	72.32(3.44)	89.57(0.10)	90.58(0.85)	88.71(1.12)	92.44(0.73)	93.17(0.60)	91.82(0.08)
MNFL [47]	69.79(2.91)	72.66(2.02)	67.28(2.01)	89.41(0.84)	89.87(0.63)	88.52(0.94)	93.38(0.36)	93.46(0.34)	92.81(0.39)
EPs-stacking [33]	73.05(1.95)	75.77(1.44)	70.80(2.10)	83.62(1.54)	84.99(0.98)	82.30(1.65)	88.17(0.41)	89.01(0.43)	87.20(0.45)
EPs-F	<b>82.72</b> (2.22)	<b>84.00</b> (1.90)	<b>81.31</b> (2.41)	<b>93.81</b> (0.94)	<b>94.09</b> (0.79)	<b>93.32</b> (0.14)	<b>96.26</b> (0.53)	<b>96.46</b> (0.49)	<b>95.96</b> (0.58)

the sixth class (Bare soil) of the classification map obtained by the EPs-stacking method. By contrast, the proposed EPs-F method can provide the best visual performance at these areas, with great suppression on noise. The corresponding quantitative results are shown in Table III with the best results in bold. As can be seen, compared with the SVM-CK, GCK-MLR, SC-MK, and MNFL methods, the average improvements of the proposed method are over 2.1%, 1.7%, and 2.7%, in terms of OA, AA, and K, respectively.

In addition, another experiment is conducted on the Houston University image, with different numbers of randomly selected

training samples (i.e., 10, 30, and 50 training samples for each class, respectively) to evaluate the performance of the investigated methods. The quantitative results are represented in Table IV with the best results in bold. As can be observed, the proposed EPs-F method outperforms all the compared methods in terms of OA, AA, and K even if only a small number of training samples are available. The main reasons are twofold. On the one hand, the EP can well preserve the geometrical characteristics of the HSI, which can offer a discriminative information for classification. On the other hand, by fusing the abundant spatial information within

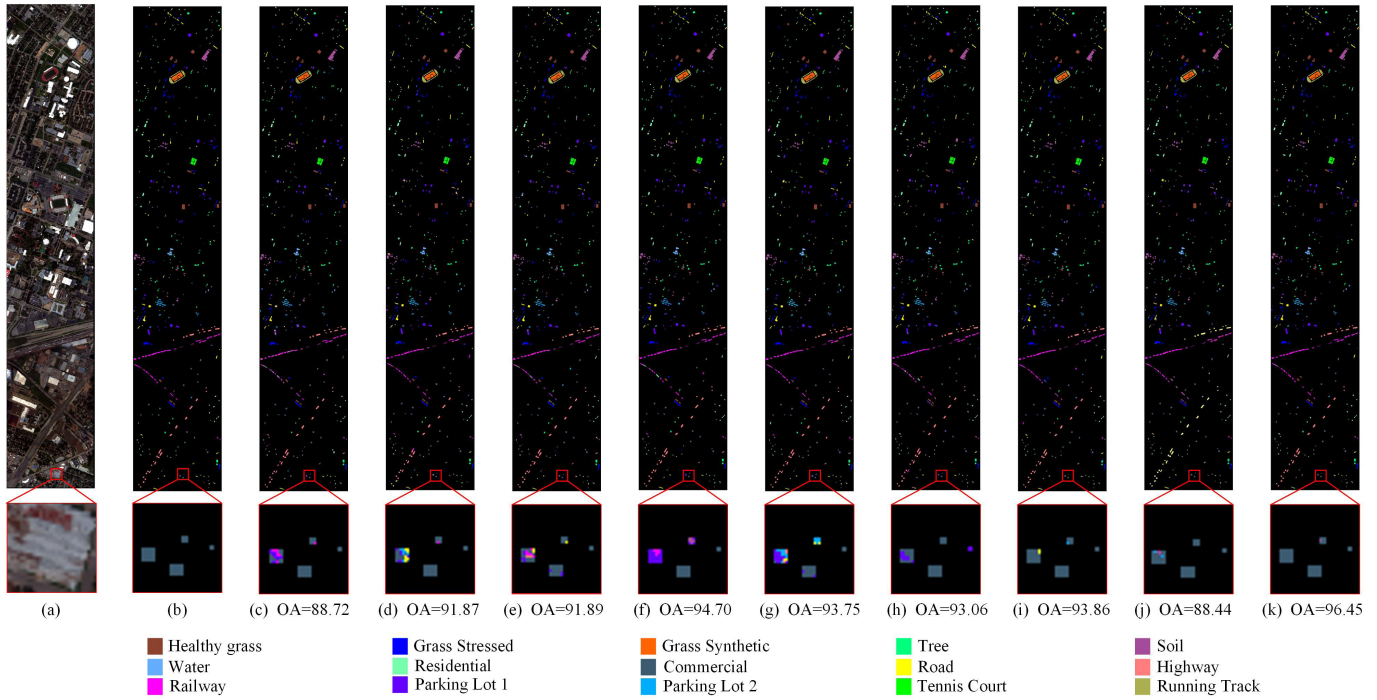


Fig. 7. Reference map and classification results (%) for the Houston University image. (a) False-color composite images. (b) Reference. (c) SVM [16]. (d) EMP [29]. (e) SVM-CK [19]. (f) EPF [46]. (g) GCK-MLR [20]. (h) SC-MK [21]. (i) MNFL [47]. (j) EPs-stacking [33]. (k) Proposed EPs-F.

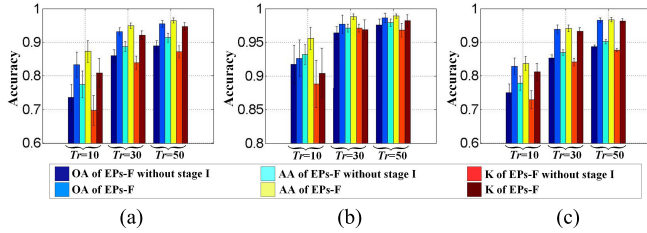


Fig. 8. Classification result (in OA, AA, and K) comparison between EPs-F and EPs-F without Fusion Stage I using various number of training samples. (a) Indian Pines image. (b) University of Pavia image. (c) Houston University image.

each EP (i.e., Fusion Stage I) and incorporating the complementary information among EPs (i.e., Fusion Stage II), the discriminative information is sufficiently utilized. The visual performance comparison of different methods with  $Tr = 50$  is represented in Fig. 7. As can be seen, the proposed EPs-F method provides the best visual classification result compared with other test methods (see the zoomed-in regions of Fig. 7).

*D. Effects of Fusion Stages I and II*

This section analyzes the effects of Fusion Stages I and II in the proposed EPs-F algorithm.

1) *Effect of Fusion Stage I:* The step of spatial information extraction within EP is removed and the three complementary EPs are directly combined together to create a composite kernel for classification while other parameters and operations remain unchanged. The corresponding classification performance is compared with the proposed EPs-F on various images, which is illustrated in Fig. 8. As can be observed, the proposed method delivers a better classification performance on different images considering various numbers of

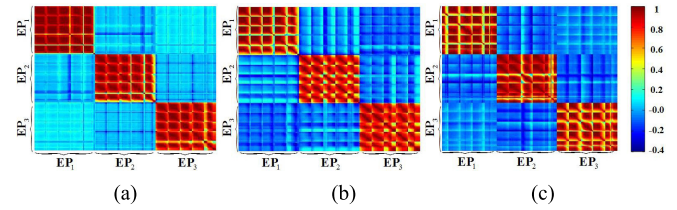


Fig. 9. Correlation coefficient matrices across different EPs for the three test HSI images. (a) Indian Pines. (b) University of Pavia. (c) Houston University.

training samples. Specifically, for the Indian Pines data sets, the classification accuracy decreases when Fusion Stage I is removed. When only ten training samples are selected for each class (i.e.,  $Tr = 10$ ), the OA of the proposed EPs-F method is 83.35%, while the OA of the EPs-F without stage I is 73.58%, which are shown in Table V with the best results in bold. It can be seen that the OA decreases by almost 10%. The main reason is that without Fusion Stage I, the abundant spatial information within each EP cannot be well exploited. The same situation can also be observed for the University of Pavia data sets and Houston University data sets. Overall, the proposed fusion frameworks can consistently achieve the best results in terms of classification accuracies when the spatial information within EP is effectively exploited.

2) *Effect of Fusion Stage II:* First, the complementary properties between different EPs are investigated. Fig. 9 shows the correlation coefficient matrix across the different EPs on the three test images and the bar in the last column represents the correlation value in the coefficient matrix. As can be observed, the correlations within each EP are very strong, while different EPs have much smaller correlations. These low correlations among EPs just show the differences while still

TABLE V  
AA (STANDARD DEVIATION) (%) OF TEN REPEATED EXPERIMENTS  
ON THREE TEST IMAGES OBTAINED BY EPS-F AND ITS  
TWO VARIANT METHODS

Indian Pines					
Method	EPs-F without Fusion Stage I	EPs-F without Fusion Stage II			EPs-F
		EP <sub>1</sub>	EP <sub>2</sub>	EP <sub>3</sub>	
OA	73.58	78.55	78.89	79.92	<b>83.35</b>
	(3.42)	(2.93)	(3.24)	(5.52)	(3.34)
AA	82.72	84.13	84.79	82.63	<b>87.28</b>
	(3.98)	(4.20)	(2.80)	(3.43)	(3.98)
K	75.40	75.80	76.63	80.63	<b>80.85</b>
	(4.41)	(5.24)	(3.69)	(4.67)	(4.31)
University of Pavia					
Method	EPs-F without Fusion Stage I	EPs-F without Fusion Stage II			EPs-F
		EP <sub>1</sub>	EP <sub>2</sub>	EP <sub>3</sub>	
OA	91.44	88.82	89.59	86.11	<b>92.56</b>
	(2.72)	(2.34)	(2.60)	(4.84)	(2.56)
AA	93.14	90.63	3.55	91.83	<b>95.53</b>
	(1.44)	(1.52)	(1.64)	(2.32)	(1.50)
K	88.91	85.53	86.62	83.41	<b>90.33</b>
	(3.42)	(2.93)	(3.24)	(5.52)	(3.34)
Houston University					
Method	EPs-F without Fusion Stage I	EPs-F without Fusion Stage II			EPs-F
		EP <sub>1</sub>	EP <sub>2</sub>	EP <sub>3</sub>	
OA	74.95	75.91	78.37	81.00	<b>82.72</b>
	(2.32)	(3.35)	(2.66)	(2.11)	(2.22)
AA	77.65	77.86	80.30	82.45	<b>84.00</b>
	(2.00)	(3.03)	(2.16)	(1.66)	(1.90)
K	72.92	74.03	76.63	79.52	<b>81.31</b>
	(2.52)	(3.24)	(2.92)	(2.32)	(2.42)

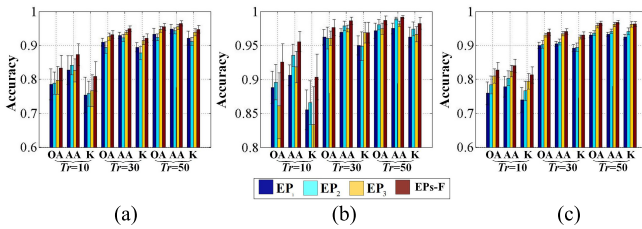


Fig. 10. Classification results (in OA, AA, and K) comparison between EPs-F and EPs-F without Fusion Stage II at various number of training samples. (a) Indian Pines image. (b) University of Pavia image. (c) Houston University image.

be complementary. Note that, given a matrix  $X = [x_1, x_2, \dots, x_n]$ , its correlation coefficient matrix  $R \in \mathbb{R}^{n \times n}$  is calculated by

$$R(i, j) = \frac{\text{cov}(x_i, x_j)}{\sqrt{\text{cov}(x_i, x_i) \times \text{cov}(x_j, x_j)}} \quad (16)$$

where cov denotes the covariance operation. Then, each EP is regarded as an independent feature and only spatial information within each EP is considered to create the classification result. The parameters and operation are similar to the EPs-F. Fig. 10 shows the classification result comparison between EPs-F and EPs-F without Fusion Stage II on different images and number of training samples. As can be seen, by utilizing the complementary information among different EPs with the MV, the classification performance of the proposed EPs-F method outperforms other single features (i.e., EP<sub>1</sub>, EP<sub>2</sub>, and EP<sub>3</sub>) and the advantage of the proposed method

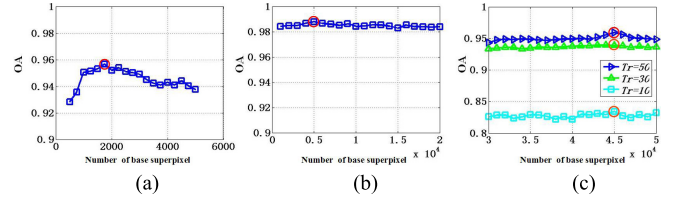


Fig. 11. Effects of the number of base superpixels on three different images. (a) Indian Pines image (Tr = 50). (b) University of Pavia image (Tr = 50). (c) Houston University image (Tr = 10, Tr = 30, and Tr = 50).

becomes more obvious when the available training samples are limited (e.g., Tr = 10). For example, as shown in Table V, for the University of Pavia data sets, the proposed method has the highest classification accuracy with OA = 92.56%, whereas the OAs of other single features (i.e., EP<sub>1</sub>, EP<sub>2</sub>, and EP<sub>3</sub>) are 88.82%, 89.59%, and 86.11% with the decrease of 3.74%, 2.97%, and 6.45%, respectively. The same results can also be observed on the other two data sets (e.g., Indian Pines and Houston University), which demonstrate that the MV can utilize the complementary information among different EPs in our proposed fusion framework for classification. Note that the best results in Table V are shown in bold.

### E. Parameter Discussion

1) *Effects of Number of Base Superpixel*: In this section, the effect of the number of base superpixels is investigated. The numbers of training and test samples are selected to be the same as in the aforementioned experiments on the Indian Pines image, University of Pavia images, and Houston University image.

According to the size of the image, the number of base superpixels for the Indian Pines image is selected from 500 to 5000 with the step size of 250. The number of base superpixels for the University of Pavia image is selected from 1000 to 20000 with the step size of 1000, while the number of base superpixels on the Houston University image is selected from 30000 to 50000 with the step size of 1000. Fig. 11 illustrates the OA values of the proposed EPs-F method under different base superpixel numbers on all three test images. Specifically, for Indian Pines, as can be observed, the classification accuracy of the OA reaches the best when the superpixel number is equal to 1750 (marked by a red circle) and the OA decreases when the number of base superpixels is selected to be other values. This is mainly due to the fact that when the number of base superpixels is less than 1750, the spatial information with different classes might be included into one superpixel, and thus, it leads to the decrease in the classification accuracy. On the other hand, when the number of base superpixels is larger than 1750, the size of each superpixel will become small, and thus, the spatial information (e.g., in large homogeneous regions of the Indian Pines image) will not be sufficiently exploited for classification.

In addition, the same situation can also be seen on other test two images (i.e., the University of Pavia and Houston University) with the optimal number of base superpixels 5000 and 45000, respectively. Note that, with different number of training samples, the best number of base superpixels

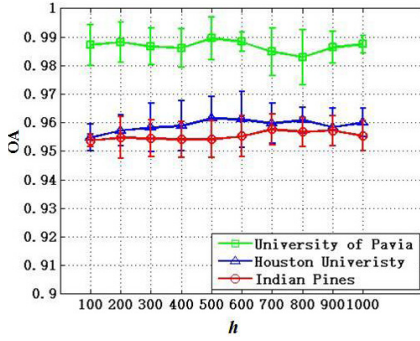


Fig. 12. Effects of the parameter  $h$  in (10) to the classification accuracy on three test images with  $Tr = 50$ .

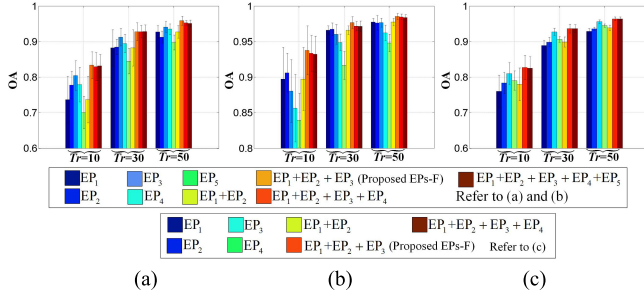


Fig. 13. Effects of the weight's distribution in (10) to the classification accuracy on three test images with different values of  $Tr$ . (a) Indian Pines. (b) University of Pavia. (c) Houston University.

for Houston university is the same [see Fig. 11(c)], which demonstrates the robustness of the proposed method.

2) *Effect of Parameter  $h$* : The proposed method is tested on three test images with  $h$  varied from 100 to 1000 (with  $Tr = 50$ ), which is shown in Fig. 12. As can be observed, the classification results on the three test images remain comparatively stable. For example, on the Indian Pines image, the difference between the maximum OA and the minimum OA is less than 0.5%. Moreover, since the University of Pavia and Houston University images are acquired from the urban area with more detailed structures, the optimal  $h$  values for the University of Pavia and Houston University images are smaller than the  $h$  for Indian Pines. The optimal  $h$  for the Indian Pines, University of Pavia, and Houston University is 700, 500, and 500, respectively, and  $h$  is set to be 500 for these three images.

#### F. Effect of Different Number of EP Groups

In this section, the influence of the number of EP groups on the proposed EPs-F method is investigated. Specifically, for the Indian Pines and Pavia University images, the first five EPs are generated with the first five ICs, and each of them as well as their combinations are analyzed. Also, for the Houston University image, the first four EPs are generated with the first four ICs, and each of them as well as their combinations are analyzed. Fig. 13 illustrates the classification results of the proposed method with different EP groups on three test images of different training samples. As can be observed, utilizing  $EP_1 + EP_2 + EP_3$  (proposed EPs-F) almost delivers

the best classification results. Further utilizing more EPs does not show any improvements and even deteriorate the performance. Therefore, in this paper, the first three ICs are utilized.

Overall, by considering three different images with diverse characteristics (i.e., spatial and spectral resolution) and training samples, the first three ICs can always deliver the best performance. Therefore, only three ICs are expected to lead to very good results and it is not necessary to adjust this parameter if other images are used.

## V. CONCLUSION

In this paper, a new two-step-based fusion framework is proposed to exploit the spatial information of the EP for HSI classification, which is termed the EPs-F method. First, by extracting the EP from first three ICs of the HSI, three discriminative and complementary EPs can be constructed. Then, a superpixel-based adaptive composite kernel strategy is proposed to incorporate the spatial information within each EP and spectral features of the original HSI image. Furthermore, a decision fusion strategy is utilized to fuse complementary information among EPs. In this way, the abundant spatial information within each EP, the spectral feature of the original HSI, and the complementary information among EPs are well utilized. The classification results obtained by the proposed EPs-F on three real HSIs outperform several state-of-the-art classification methods in terms of quantitative and visual performance that proves the effectiveness of the proposed method.

In the proposed framework, the superpixel-based method is used to explore the abundant information within the EP. However, since the EP is also a 3-D image, the tensor analysis-based method deserves to be studied to extract more discriminative features for classification. Moreover, our future work will utilize other kinds of features and combine them with EPs to improve classification accuracies.

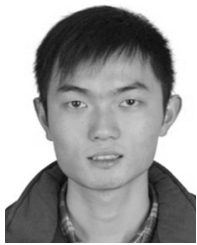
## ACKNOWLEDGMENT

The authors would like to thank Prof. D. Landgrebe from Purdue University and the NASA Jet Propulsion Laboratory for providing the free downloads of the hyperspectral data sets. They would like to thank Dr. J. Li for providing the software of generalized composite kernel-based multivariate logistic regression and MNFL. They would also like to thank the editors and anonymous reviewers for their insightful comments and suggestions, which have significantly improved this paper.

## REFERENCES

- [1] M. Dalponte, H. O. Orka, T. Gobakken, D. Gianelle, and E. Naeset, "Tree species classification in boreal forests with hyperspectral data," *IEEE Trans. Geosci. Remote Sens.*, vol. 51, no. 5, pp. 2632–2645, May 2013.
- [2] K. Karalakis, G. Tsagkatakis, M. Zervakis, and P. Tsakalides, "Land classification using remotely sensed data: Going multilabel," *IEEE Trans. Geosci. Remote Sens.*, vol. 54, no. 6, pp. 3548–3563, Jun. 2016.
- [3] J. M. Bioucas-Dias, A. Plaza, G. Camps-Valls, P. Scheunders, N. M. Nasrabadi, and J. Chanussot, "Hyperspectral remote sensing data analysis and future challenges," *IEEE Geosci. Remote Sens. Mag.*, vol. 1, no. 2, pp. 6–36, Jun. 2013.

- [4] F. Ratle, G. Camps-Valls, and J. Weston, "Semisupervised neural networks for efficient hyperspectral image classification," *IEEE Trans. Geosci. Remote Sens.*, vol. 48, no. 5, pp. 2271–2282, May 2010.
- [5] Q. Wang, Y. Gu, and D. Tuia, "Discriminative multiple kernel learning for hyperspectral image classification," *IEEE Trans. Geosci. Remote Sens.*, vol. 54, no. 7, pp. 3912–3927, Jul. 2016.
- [6] Y. Gu, J. Chanussot, X. Jia, and J. A. Benediktsson, "Multiple kernel learning for hyperspectral image classification: A review," *IEEE Trans. Geosci. Remote Sens.*, vol. 55, no. 11, pp. 6547–6565, Nov. 2017.
- [7] Y. Gu, T. Liu, X. Jia, J. A. Benediktsson, and J. Chanussot, "Nonlinear multiple kernel learning with multiple-structure-element extended morphological profiles for hyperspectral image classification," *IEEE Trans. Geosci. Remote Sens.*, vol. 54, no. 6, pp. 3235–3247, Jun. 2016.
- [8] S. Jia, L. Shen, and Q. Li, "Gabor feature-based collaborative representation for hyperspectral imagery classification," *IEEE Trans. Geosci. Remote Sens.*, vol. 53, no. 2, pp. 1118–1129, Feb. 2015.
- [9] J. Liu, Z. Wu, J. Li, A. Plaza, and Y. Yuan, "Probabilistic-kernel collaborative representation for spatial-spectral hyperspectral image classification," *IEEE Trans. Geosci. Remote Sens.*, vol. 54, no. 4, pp. 2371–2384, Apr. 2016.
- [10] L. Fang, S. Li, X. Kang, and J. A. Benediktsson, "Spectral-spatial hyperspectral image classification via multiscale adaptive sparse representation," *IEEE Trans. Geosci. Remote Sens.*, vol. 52, no. 12, pp. 7738–7749, Dec. 2014.
- [11] L. Fang, C. Wang, S. Li, and J. A. Benediktsson, "Hyperspectral image classification via multiple-feature-based adaptive sparse representation," *IEEE Trans. Instrum. Meas.*, vol. 66, no. 7, pp. 1646–1657, Jul. 2017.
- [12] L. Fang, S. Li, X. Kang, and J. A. Benediktsson, "Spectral-spatial classification of hyperspectral images with a superpixel-based discriminative sparse model," *IEEE Trans. Geosci. Remote Sens.*, vol. 53, no. 8, pp. 4186–4201, Aug. 2015.
- [13] S. Jia, J. Hu, Y. Xie, L. Shen, X. Jia, and Q. Li, "Gabor cube selection based multitask joint sparse representation for hyperspectral image classification," *IEEE Trans. Geosci. Remote Sens.*, vol. 54, no. 6, pp. 3174–3187, Jun. 2016.
- [14] L. Fang, S. Li, D. Cunefare, and S. Farsiu, "Segmentation based sparse reconstruction of optical coherence tomography images," *IEEE Trans. Med. Imag.*, vol. 36, no. 2, pp. 407–421, Feb. 2017.
- [15] L. Fang, D. Cunefare, C. Wang, R. H. Guymer, S. Li, and S. Farsiu, "Automatic segmentation of nine retinal layer boundaries in OCT images of non-exudative AMD patients using deep learning and graph search," *Biomed. Opt. Exp.*, vol. 8, no. 5, pp. 2732–2744, May 2017.
- [16] F. Melgani and L. Bruzzone, "Classification of hyperspectral remote sensing images with support vector machines," *IEEE Trans. Geosci. Remote Sens.*, vol. 42, no. 8, pp. 1778–1790, Aug. 2004.
- [17] L. Bruzzone, M. Chi, and M. Marconcini, "A novel transductive SVM for semisupervised classification of remote-sensing images," *IEEE Trans. Geosci. Remote Sens.*, vol. 44, no. 11, pp. 3363–3373, Nov. 2006.
- [18] M. Fauvel, J. Chanussot, and J. A. Benediktsson, "Evaluation of kernels for multiclass classification of hyperspectral remote sensing data," in *Proc. IEEE Int. Conf. Acoust., Speech Signal Process.*, May 2006, p. 2.
- [19] G. Camps-Valls, L. Gomez-Chova, J. Munoz-Mari, J. Vila-Frances, and J. Calpe-Maravilla, "Composite kernels for hyperspectral image classification," *IEEE Geosci. Remote Sens. Lett.*, vol. 3, no. 1, pp. 93–97, Jan. 2006.
- [20] J. Li, P. R. Marpu, A. Plaza, J. M. Bioucas-Dias, and J. A. Benediktsson, "Generalized composite kernel framework for hyperspectral image classification," *IEEE Trans. Geosci. Remote Sens.*, vol. 51, no. 9, pp. 4816–4829, Sep. 2013.
- [21] L. Fang, S. Li, W. Duan, J. Ren, and J. A. Benediktsson, "Classification of hyperspectral images by exploiting spectral-spatial information of superpixel via multiple kernels," *IEEE Trans. Geosci. Remote Sens.*, vol. 53, no. 12, pp. 6663–6674, Dec. 2015.
- [22] X. Kang, S. Li, and J. A. Benediktsson, "Feature extraction of hyperspectral images with image fusion and recursive filtering," *IEEE Trans. Geosci. Remote Sens.*, vol. 52, no. 6, pp. 3742–3752, Jun. 2014.
- [23] S. Prasad and L. M. Bruce, "Limitations of principal components analysis for hyperspectral target recognition," *IEEE Geosci. Remote Sens. Lett.*, vol. 5, no. 4, pp. 625–629, Oct. 2008.
- [24] A. Villa, J. A. Benediktsson, J. Chanussot, and C. Jutten, "Hyperspectral image classification with independent component discriminant analysis," *IEEE Trans. Geosci. Remote Sens.*, vol. 49, no. 12, pp. 4865–4876, Dec. 2011.
- [25] W. Li, S. Prasad, J. E. Fowler, and L. M. Bruce, "Locality-preserving dimensionality reduction and classification for hyperspectral image analysis," *IEEE Trans. Geosci. Remote Sens.*, vol. 50, no. 4, pp. 1185–1198, Apr. 2012.
- [26] P. Ghamisi, J. A. Benediktsson, and M. O. Ulfarsson, "Spectral-spatial classification of hyperspectral images based on hidden Markov random fields," *IEEE Trans. Geosci. Remote Sens.*, vol. 52, no. 5, pp. 2565–2574, May 2014.
- [27] X. Jia and J. A. Richards, "Managing the spectral-spatial mix in context classification using Markov random fields," *IEEE Geosci. Remote Sens. Lett.*, vol. 5, no. 2, pp. 311–314, Apr. 2008.
- [28] J. A. Benediktsson, M. Pesaresi, and K. Amason, "Classification and feature extraction for remote sensing images from urban areas based on morphological transformations," *IEEE Trans. Geosci. Remote Sens.*, vol. 41, no. 9, pp. 1940–1949, Sep. 2003.
- [29] J. A. Benediktsson, J. A. Palmason, and J. R. Sveinsson, "Classification of hyperspectral data from urban areas based on extended morphological profiles," *IEEE Trans. Geosci. Remote Sens.*, vol. 43, no. 3, pp. 480–491, Mar. 2005.
- [30] A. Plaza, P. Martinez, J. Plaza, and R. Perez, "Dimensionality reduction and classification of hyperspectral image data using sequences of extended morphological transformations," *IEEE Trans. Geosci. Remote Sens.*, vol. 43, no. 3, pp. 466–479, Mar. 2005.
- [31] M. Dalla Mura, J. A. Benediktsson, B. Waske, and L. Bruzzone, "Morphological attribute profiles for the analysis of very high resolution images," *IEEE Trans. Geosci. Remote Sens.*, vol. 48, no. 10, pp. 3747–3762, Oct. 2010.
- [32] P. Ghamisi, R. Souza, J. A. Benediktsson, X. X. Zhu, L. Rittner, and R. A. Lotufo, "Extinction profiles for the classification of remote sensing data," *IEEE Trans. Geosci. Remote Sens.*, vol. 54, no. 10, pp. 5631–5645, Oct. 2016.
- [33] P. Ghamisi, R. Souza, J. A. Benediktsson, L. Rittner, R. Lotufo, and X. X. Zhu, "Hyperspectral data classification using extended extinction profiles," *IEEE Geosci. Remote Sens. Lett.*, vol. 13, no. 11, pp. 1641–1645, Nov. 2016.
- [34] P. Comon, "Independent component analysis: A new concept?" *Signal Process.*, vol. 36, no. 3, pp. 287–314, Apr. 1994.
- [35] M.-Y. Liu, O. Tuzel, S. Ramalingam, and R. Chellappa, "Entropy rate superpixel segmentation," in *Proc. IEEE Conf. Comput. Vis. Pattern Recognit.*, Jun. 2011, pp. 2097–2104.
- [36] C. Vachier and F. Meyer, "Extinction value: A new measurement of persistence," in *Proc. IEEE Workshop Nonlinear Signal Image Process.*, Jun. 1995, pp. 254–257.
- [37] P. Soille, *Morphological Image Analysis: Principles and Applications*, 2nd ed. Secaucus, NJ, USA: Springer-Verlag, 2003.
- [38] W. Fu, S. Li, and L. Fang, "Spectral-spatial hyperspectral image classification via superpixel merging and sparse representation," in *Proc. IEEE Int. Geosci. Remote Sens. Symp. (IGARSS)*, Jul. 2015, pp. 4971–4974.
- [39] R. Roscher and B. Waske, "Superpixel-based classification of hyperspectral data using sparse representation and conditional random fields," in *Proc. IEEE Int. Geosci. Remote Sens. Symp. (IGARSS)*, Jul. 2014, pp. 3674–3677.
- [40] J. Liu, W. Yang, S. Tan, and Z. Wang, "Remote sensing image classification based on random projection super-pixel segmentation," *Proc. SPIE*, vol. 8921, pp. 2633–2638, Oct. 2013.
- [41] T. Lu, S. Li, L. Fang, L. Bruzzone, and J. A. Benediktsson, "Set-to-set distance-based spectral-spatial classification of hyperspectral images," *IEEE Trans. Geosci. Remote Sens.*, vol. 54, no. 12, pp. 7122–7134, Dec. 2016.
- [42] S. Li, T. Lu, L. Fang, X. Jia, and J. A. Benediktsson, "Probabilistic fusion of pixel-level and superpixel-level hyperspectral image classification," *IEEE Trans. Geosci. Remote Sens.*, vol. 54, no. 12, pp. 7416–7430, Dec. 2016.
- [43] L. Fang, H. Zhuo, and S. Li, "Super-resolution of hyperspectral image via superpixel-based sparse representation," *Neurocomputing*, vol. 273, no. 1, pp. 171–177, Jan. 2018.
- [44] I. Jolliffe, *Principal Component Analysis*. New York, NY, USA: Wiley, 2005.
- [45] J. Canny, "A computational approach to edge detection," *IEEE Trans. Pattern Anal. Mach. Intell.*, vol. PAMI-8, no. 6, pp. 200–209, Nov. 1986.
- [46] X. Kang, S. Li, and J. A. Benediktsson, "Spectral-spatial hyperspectral image classification with edge-preserving filtering," *IEEE Trans. Geosci. Remote Sens.*, vol. 52, no. 5, pp. 2666–2677, May 2014.
- [47] J. Li *et al.*, "Multiple feature learning for hyperspectral image classification," *IEEE Trans. Geosci. Remote Sens.*, vol. 53, no. 3, pp. 1592–1606, Mar. 2015.



**Leyuan Fang** (S'10–M'14–SM'17) received the B.S. and Ph.D. degrees from the College of Electrical and Information Engineering, Hunan University, Changsha, China, in 2008 and 2015, respectively.

From 2011 to 2012, he was a Visiting Ph.D. Student with the Department of Ophthalmology, Duke University, Durham, NC, USA, supported by the China Scholarship Council. Since 2017, he has been an Associate Professor with the College of Electrical and Information Engineering, Hunan University. His research interests include sparse representation and multiresolution analysis in remote sensing and medical image processing.

Dr. Fang received the Scholarship Award for the Excellent Doctoral Student from the Chinese Ministry of Education in 2011.



**Nanjun He** (S'17) received the B.S. degree from the Central South University of Forestry and Technology, Changsha, China, in 2013. He is currently pursuing the Ph.D. degree with the Laboratory of Vision and Image Processing, Hunan University, Changsha.

Since 2017, he has been a Visiting Ph.D. Student with the Hyperspectral Computing Laboratory, University of Extremadura, Cáceres, Spain, supported by the China Scholarship Council. His research interests include hyperspectral imagery classification, hyperspectral imagery restoration, and computer vision in remote sensing images.

computer vision in remote sensing images.



**Shutao Li** (M'07–SM'15) received the B.S., M.S., and Ph.D. degrees from Hunan University, Changsha, China, in 1995, 1997, and 2001, respectively.

He was a Research Associate with the Department of Computer Science, The Hong Kong University of Science and Technology, Hong Kong, in 2011. From 2002 to 2003, he was a Post-Doctoral Fellow with the Royal Holloway College, University of London, London, U.K., under the supervision of Prof. J. Shawe-Taylor. In 2005, he was a Visiting Professor with the Department of Computer Science, The Hong Kong University of Science and Technology. He joined the College of Electrical and Information Engineering, Hunan University, in 2001, where he is currently a Full Professor. He has authored or co-authored over 160 refereed papers. His research interests include compressive sensing, sparse representation, image processing, and pattern recognition.

Dr. Li is a member of the Editorial Board of the *Information Fusion and the Sensing and Imaging*. He is currently an Associate Editor of the *IEEE TRANSACTIONS ON GEOSCIENCE AND REMOTE SENSING* and the *IEEE TRANSACTIONS ON INSTRUMENTATION AND MEASUREMENT*. He was a recipient of two Second-Grade National Awards at the Science and Technology Progress of China in 2004 and 2006, respectively.



**Pedram Ghamisi** (S'12–M'15) received the B.Sc. degree in civil (survey) engineering from the Tehran South Campus of Azad University, Tehran, Iran, the M.Sc. degree (Hons.) in remote sensing from the K. N. Toosi University of Technology, Tehran, in 2012, and the Ph.D. degree in electrical and computer engineering from the University of Iceland, Reykjavik, Iceland, in 2015.

From 2013 to 2014, he spent seven months with the School of Geography, Planning and Environmental Management, The University of Queensland, Brisbane, QLD, Australia. He was a Post-Doctoral Research Fellow with the University of Iceland. He has been a Post-Doctoral Research Fellow with the Technische Universität München, München, Germany, and Heidelberg University, Heidelberg, Germany, since 2015. He has also been a Researcher with the German Aerospace Center, Remote Sensing Technology Institute, Wessling, Germany, since 2015. His research interests include remote sensing and image analysis, with a special focus on spectral and spatial techniques for hyperspectral image classification, multisensor data fusion, machine learning, and deep learning.

Dr. Ghamisi received the prestigious Alexander von Humboldt Fellowship in 2015. In the 2010–2011 academic year, he received the Best Researcher Award for M.Sc. students from the K. N. Toosi University of Technology. In 2013, he presented at the IEEE International Geoscience and Remote Sensing Symposium, Melbourne, VIC, Australia, and received the IEEE Mikio Takagi Prize for winning the conference Student Paper Competition against almost 70 people. In 2016, he was selected as a Talented International Researcher by the Iran's National Elites Foundation. In 2017, he won the Data Fusion Contest 2017 organized by the Image Analysis and Data Fusion Technical Committee of the IEEE Geoscience and Remote Sensing Society. His model was the most accurate among over 800 submissions.



**Jón Atli Benediktsson** (S'84–M'90–SM'99–F'04) received the Cand.scient. degree from the University of Iceland, Reykjavik, Iceland, in 1984, and the M.S.E.E. and Ph.D. degrees from Purdue University, West Lafayette, IN, USA, in 1987 and 1990, respectively, all in electrical engineering.

From 2009 to 2015, he was the Pro Rector of Science and Academic Affairs and a Professor of electrical and computer engineering with the University of Iceland. In 2015, he became the Rector of the University of Iceland. He is the Co-Founder of

a biomedical startup company Oxymap. He has authored extensively in his fields of interest. His research interests include remote sensing, image analysis, pattern recognition, biomedical analysis of signals, and signal processing.

Dr. Benediktsson is a member of the Association of Chartered Engineers at Iceland (VFI), the Societas Scientiarum Islandica, and the Tau Beta Pi. He is a fellow of the International Society for Optics and Photonics. He was the President of the IEEE Geoscience and Remote Sensing Society (GRSS) from 2011 to 2012. He has been on the GRSS Administrative Committee since 2000. He was the Chairman of the Steering Committee of the IEEE JOURNAL OF SELECTED TOPICS IN APPLIED EARTH OBSERVATIONS AND REMOTE SENSING from 2007 to 2010. He serves on the Editorial Board of the IEEE Proceedings and the International Editorial Board of the *International Journal of Image and Data Fusion*. He was a recipient of the Stevan J. Kristof Award from Purdue University in 1991 as an Outstanding Graduate Student in remote sensing. He was also a recipient of the Icelandic Research Council's Outstanding Young Researcher Award in 1997, the IEEE Third Millennium Medal in 2000, the Yearly Research Award from the Engineering Research Institute at the University of Iceland in 2006, the Outstanding Service Award from the IEEE Geoscience and Remote Sensing Society in 2007, and the IEEE/VFI Electrical Engineer of the Year Award in 2013. He was a co-recipient of the University of Iceland's Technology Innovation Award in 2004, the 2012 IEEE TRANSACTIONS ON GEOSCIENCE AND REMOTE SENSING Paper Award, the IEEE GRSS Highest Impact Paper Award in 2013, and the *International Journal of Image and Data Fusion* Best Paper Award in 2014. He was the Editor-in-Chief of the IEEE TRANSACTIONS ON GEOSCIENCE AND REMOTE SENSING (TGRS) from 2003 to 2008. He has been an Associate Editor of TGRS since 1999, the IEEE GEOSCIENCE AND REMOTE SENSING LETTERS since 2003, and the IEEE ACCESS since 2013.